

Carbon Isotope Ratio in $^{12}\text{CO}/^{13}\text{CO}$ toward Local Molecular Clouds with Near-Infrared High Resolution Spectroscopy of Vibrational Transition Bands¹

Miwa Goto,^{2,3} Tomonori Usuda,² Naruhisa Takato,² Masa Hayashi,² Seiichi Sakamoto,⁴ W. Gaessler,^{2,5} Yutaka Hayano,⁴ Masanori Iye,⁴ Yukiko Kamata,⁴ Tomio Kanzawa,² Naoto Kobayashi,² Yosuke Minowa,⁶ Ko Nedachi,² Shin Oya,² T.-S. Pyo,² D. Saint-Jacques,⁷ Hiroshi Suto,² Hideki Takami,² Hiroshi Terada,² A. T. Tokunaga,⁸ George F. Mitchell⁹

mgoto@duke.ifa.hawaii.edu

ABSTRACT

We report the carbon monoxide isotope ratio in local molecular clouds toward LkH α 101, AFGL 490, and Mon R2 IRS 3. The vibrational transition bands of ^{12}CO $\nu = 2 \leftarrow 0$ and ^{13}CO $\nu = 1 \leftarrow 0$ were observed with high resolution near-infrared spectroscopy ($R = 23,000$) to measure $^{12}\text{CO}/^{13}\text{CO}$ ratio. The isotopic ratios are $^{12}\text{CO}/^{13}\text{CO} = 137 \pm 9$ (LkH α 101), 86 ± 49 (AFGL 490), and 158 (Mon R2 IRS 3), which are 1.5 to 2.8 times higher than the local interstellar medium value of $^{12}\text{CO}/^{13}\text{CO} = 57 \pm 5$ from millimeter C ^{18}O emission observations. This is not easily explained by saturation of the ^{13}CO absorption. It is also questionable that the selective photo-destruction of ^{13}CO can account for the

¹Based on data collected at Subaru Telescope, which is operated by the National Astronomical Observatory of Japan.

²Subaru Telescope, 650 North A'ohoku Place, Hilo, HI 96720.

³Visiting astronomer at the Institute for Astronomy, University of Hawaii, 640 North A'ohoku Place Hilo, HI 96720.

⁴National Astronomical Observatory of Japan, Mitaka, Tokyo 181-8588, Japan.

⁵Max-Planck-Institut für Astronomie, Königstuhl 17, Heidelberg D-69117, Germany.

⁶University of Tokyo, Mitaka, Tokyo 181-0015, Japan.

⁷Groupe d'astrophysique, Université de Montréal, 2900 Boul. Édouard-Monpetit, Montréal (Québec) H3C 3J7, Canada.

⁸Institute for Astronomy, University of Hawaii, 2680 Woodlawn Dr., Honolulu, HI 96822.

⁹Department of Astronomy and Physics, Saint Mary's University, Halifax, NS B3H 3C3, Canada.

difference between the Galactic trend and the present observation, because the molecular clouds are with high visible extinction ($A_V = 10\text{--}70$ mag), well shielded from destructive FUV radiation. The molecular gas associated with AFGL 490 and Mon R2 IRS 3 consist of multiple temperature components lying in the lines of sights. In the cool component ($T_{\text{ex}} < 100$ K), the excitation temperature of ^{12}CO is twice that of ^{13}CO . We attribute the temperature discrepancy to the photon-trapping effect, which makes the radiative cooling of main isotopomer less effective.

Subject headings: infrared: ISM — ISM: abundances — ISM: clouds — ISM: lines and bands — ISM: molecules — stars: individual (LkH α 101, AFGL 490, Mon R2 IRS 3)

1. Introduction

The main isotope of carbon (^{12}C) is a primary product of the 3α process in the stellar nucleosynthesis. The rarer isotope ^{13}C has secondary origin, at least partially, produced from ^{12}C in the CNO cycle in the intermediate to high mass stars. (Wannier 1980; Prantzos, Aubert, & Audouze 1996). The cosmic isotope ratio $^{12}\text{C}/^{13}\text{C}$ decreases monotonically with time (Audouze, Lequeux, & Vigroux 1975), therefore serves as a chronological measure of the chemical enrichment of the galaxy. The isotopic ratio is more reliable than the elemental abundances because it is virtually free from the chemical and physical fractionation brought by the different elemental properties, such as the chemical reactivity and the ionization potentials.

The star forming rate is higher in the Galactic center than in the rest of the Galactic plane. The ^{13}C isotope is produced faster there, rapidly enriching the interstellar medium (ISM). The radial gradient of the isotopic ratio as a function of galactocentric distance, is thus potentially important as a touchstone of our understanding of stellar nucleosynthesis, star forming history, and injection and mixing of polluted material in the ISM (Wannier 1980; Penzias 1980; Wilson & Rood 1994; Wilson 1999).

With the large number of centimeter and millimeter wavelengths observations measuring the isotopic ratio in our Galaxy (Frerking et al. 1980; Henkel, Güsten, & Gardner 1985; Langer & Penzias 1993; Bensch et al. 2001), a positive trend of $^{12}\text{C}/^{13}\text{C}$ has gradually emerged uprising from the Galactic center to the edge of the Galaxy (Langer & Penzias 1990; Savage et al. 2002). The large scale trend allows us to infer $^{12}\text{CO}/^{13}\text{CO} = 57\pm 5$ for the solar system, 8.5 kpc from the Galactic center. The isotopic ratio in the local ISM

is particularly important because this is the only place that we know the reliable isotopic ratio of 4.5–4.7 Gyr ago. The higher $^{12}\text{C}/^{13}\text{C}$ ratio of the solar system (≈ 89 ; Anders & Grevesse 1989; Grevesse, Noels, & Sauval 1996) than that of the present-day local ISM implies the environment was less processed in the past, providing a solid evidence of the isotope enrichment by stellar nucleosynthesis and star forming activities.

However, the isotopic ratio in the solar neighborhood is still controversial. In spite of the unmistakable trend in the Galaxy, the individual measurements toward nearby molecular clouds sometimes turn out to be high with $^{12}\text{CO}/^{13}\text{CO}$ around 70 (e.g. Orion A in Langer & Penzias 1990) to 100 (e.g. NGC 2264 in Penzias 1983). The most reliable estimate of the carbon isotope ratio in the solar neighborhood is given by CH^+ molecular ions, because it is produced at high temperature, and almost free from the influence of the chemical fractionation (Watson, Anicich, & Huntress 1976). Although the isotope measurement with CH^+ is only practical for the diffuse clouds within ~ 2 kpc of the solar system, it has been extensively studied with high resolution absorption spectroscopy in the optical range (Hawkins & Jura 1987; Stahl & Wilson 1989, 1992; Hawkins, Craig, & Meyer 1993; Vladilo, Centuri3n, & C3assola 1993; Centuri3n, C3assola, & Vladilo 1996). Interestingly most of the CH^+ observations have presented high carbon isotope ratio ($^{12}\text{CH}^+ / ^{13}\text{CH}^+ = 70\text{--}90$), with best measurement toward ζ Oph being 77 ± 3 (Stahl & Wilson 1989) or 71 ± 3 (Stahl & Wilson 1992). Vladilo, Centuri3n, & C3assola (1993) reported even higher isotope ratio $^{12}\text{CH}^+ / ^{13}\text{CH}^+ = 98\text{--}120$ toward the stars in Sco OB1 association. The goal of this paper is to shed light on the conflicting carbon isotope measurements in the local ISM.

Traditionally, the emission observation in the millimeter and radio wavelengths was the favorite means to probe the carbon isotope ratio. Recently a new window has opened in the far-infrared regime for the observations of C I and C II (Boreiko & Betz 1996; Keene et al. 1998; Tieftrunk et al. 2001). The technique we employ is a near-infrared absorption spectroscopy of the carbon monoxide vibrational transition bands (Hall et al. 1978; Scoville et al. 1983; Black & Willner 1984; Mitchell et al. 1988). A bright infrared source deeply embedded in a star forming region is used as a background illumination to observe through the foreground molecular cloud. The fundamental transition of ^{12}CO is usually heavily saturated, and useless to derive any meaningful physical quantities. Instead we use the first overtone of ^{12}CO at $2.4 \mu\text{m}$ to compare with the ^{13}CO fundamental transitions at $4.7 \mu\text{m}$. The potential of the method is that the oscillator strength of the first overtone is weaker than that of the fundamental band by factor of about 140, while the isotope ratio is 50–100. Thus, the weaker transition of $^{12}\text{CO } \nu = 2 \leftarrow 0$ is therefore compensated by higher abundance. This allows spectroscopy of ^{12}CO and ^{13}CO at similar optical depth, reducing the risk of line saturation caused by the unbalanced absorption intensity without requiring a huge dynamic range in the observations.

This technique has several advantages: First, it does not rely on the double isotope ratio. To make an observation feasible under huge difference in the isotopic abundances, $^{12}\text{C}^{18}\text{O}$ is compared to $^{13}\text{C}^{16}\text{O}$, for instance, assuming any variation in $^{16}\text{O}/^{18}\text{O}$ is negligible (e.g., Wannier 1980 and references therein). The obvious caveats of this is, if there is an inverse isotopic trend in the counterpart atom, any variation in the ratio is canceled out. Second, the near-infrared spectroscopy uses the multiple transition lines simultaneously, which makes the evaluation of total column density reliable. Third, the angular resolution is nearly infinitesimal due to the point-source background. The different locations of the emitting molecules is the major obstacle in probing ^{12}CO and ^{13}CO in emission at radio wavelengths because the beam size is typically larger than $10''$ which samples gas in various physical environments. It is hard to ensure the observed ^{13}CO is exactly in the same location with ^{12}CO . Being in absorption, near-infrared spectroscopy selects the isotopomers along an identical line of sight. Fourth, the measurement is simple and robust relative to a source clean continuum. This is not the case for absorption spectroscopy in the radio and millimeter spectroscopy. For multi-line studies, there may be changes in the structure of the extended background continuum source, and there may be an emission line contribution inside the beam. A radiation transfer model used to derive the molecular abundance may introduce unknown systematic effects. The advantage and disadvantage of the techniques are reviewed in Mitchell & Maillard (1993) and Langer & Penzias (1993). In spite of these potential advances, observations utilizing near-infrared technique were sparse, with only a few examples counted to date (Scoville et al. 1983; Mitchell & Maillard 1993). This is mainly because of the difficulty of near-infrared high resolution spectroscopy ($R > 10,000$) required to separate the vibrational transition lines. It is not the case any longer with 8-m class telescopes and a new generation of instruments which includes large-format detector arrays in a cross-dispersing spectrograph.

2. Observations

The spectroscopic observations were made at the 8.2-m Subaru Telescope on 2002 December 23, 24 UT for the first overtone transitions (LkH α 101, AFGL 490, and Mon R2 IRS 3), and on 2003 February 18 UT for the fundamental transitions (LkH α 101). A facility instrument Infrared Camera and Spectrograph (IRCS; Tokunaga et al. 1998; Kobayashi et al. 2000) was used. IRCS is equipped with an echelle and a cross-dispersing gratings to offer high resolution spectroscopy yet with a wide wavelength coverage. The grating angles were set to cover 2.296–2.353 μm on December 23 and 24 to observe entire R -branch and $P(1)$ – $P(2)$ of the ^{12}CO first overtone. The gratings were readjusted to cover 4.714–4.824 μm on February 18 for the ^{13}CO fundamental band $R(0)$ – $R(5)$ and $P(1)$ – $P(6)$. An adaptive optics

(AO) system (Takami et al. 1998; Gaessler et al. 2002) was used in conjunction during the observation of LkH α 101 and Mon R2 IRS 3 to increase the slit through-put. The AO system at the Subaru Telescope is a 36-element curvature-sensing system installed at the Cassegrain port. In an average seeing night ($0''.5$ – $0''.6$ at $2.2 \mu\text{m}$) only a small fraction of the point source flux is contained in the $0''.15$ slit that is used to obtain a spectra of resolving power of $R = 23,000$. The AO system delivers a point spread function as sharp as $0''.07$ at $2 \mu\text{m}$, raising the slit through-put more than double. LkH α 101 itself and an offset guide star at $23''$ southwest of Mon R2 IRS 3 were used as the wavefront reference for the AO system. AFGL 490 was observed without AO because of the lack of close visible stars. The slit position angle was along the east to the west. The spectra were recorded by nodding the tip-tilt mirror inside the AO system by $3''$ along the slit to subtract the sky emission and dark current images. A nearby early type star HR 1791 (B7 III, $V=1.65$) was observed as a spectroscopic standard through a airmass similar to the targets. The spectroscopic flat field was obtained at the end of the night with a halogen lamp. The total on-source integration times were 8 min, 30 min, and 12 min for $^{12}\text{CO } \nu = 2 \leftarrow 0$ of LkH α 101, AFGL 490, and Mon R2 IRS 3, and 200 s for LkH α 101 $^{13}\text{CO } \nu = 1 \leftarrow 0$, respectively. We had an excellent seeing condition of $0''.3$ – $0''.4$ at $2.2 \mu\text{m}$ on December 24, and average seeing of $0''.5$ – $0''.6$ on December 23 and February 18.

3. Data Reduction and Analysis

3.1. Column Density

The spectrograms were stacked and pair-subtracted without sub-pixel registration. The shift of the spectrograms on the array detector, either because of the telescope tracking errors or of instrument flexure, was negligible compared to the spectral resolution. The pixel variation of the detector response was flattened by taking the ratio with the dark-subtracted flat-fielding images. The outlying pixels were collected based on the statistics of the flat-fielding and dark current images to make bad pixel tables. Those pixels were interpolated before the spectral extraction. We used IRAF¹⁰ aperture extraction package to obtain the one-dimensional spectra. After the extraction, a set of custom-written IDL codes were used to handle (1) linear registration of the wavelength between the object and the standard star spectra, (2) convolution of spectra to match the wavelength resolution in the object and the standard star, (3) rescaling the standard star spectrum according to Beer’s law to reduce the

¹⁰IRAF is distributed by the National Optical Astronomy Observatories, which are operated by the Association of Universities for Research in Astronomy, Inc., under cooperative agreement with the National Science Foundation.

residual features of the airmass mismatch, and (4) the wavelength calibration by maximizing the cross-correlation of the observed spectrum with a model atmospheric transmission curve calculated by ATRAN code (Lord 1992). The resultant spectra were calibrated by a ratio to the standard star. These are shown in Figure 1 and Figure 2 together with the atmospheric transmission curve convolved into the similar spectral resolution.

Typical line width of molecular clouds in the Galactic plane is $\Delta v_{\text{FWHM}} < 15 \text{ km s}^{-1}$. The individual transition lines were barely resolved with the present modest FWHM spectral resolution (13 km s^{-1}). We used the equivalent widths to measure the column density of CO. The absorption lines were fit with a Gaussian profile, and analytically integrated to the equivalent widths. One sigma error per pixel was calculated as a standard deviation of the continuum level after the Gaussian profile was subtracted. The error evaluation thus contains both statistical and fitting errors that comes from the deviant absorption profile from the Gaussian function. The standard deviation was multiplied by the square root of the number of pixels within $\pm 3 \sigma$ of the Gaussian line width.

The atmospheric transmission curve is not smooth in the wavelengths we observed, but a superposition of many telluric molecular absorption lines mainly of methane, CO and water vapor. Since neither of the interstellar or the atmospheric absorption lines were properly resolved, the observed equivalent width is a function of the wavelength where the absorption line falls, whether it was at low or high transmissive region before the spectrum is binned by the instrumental resolution. The atmospheric transmission efficiency was calculated at each wavelength of the CO absorption, referring intrinsic atmospheric transmission curve computed by ATRAN simulation code. The profile of the CO absorption line was assumed to be a Gaussian function. The Doppler parameters of the absorption lines used at the calculation were $b = 2.0 \text{ km s}^{-1}$ ($= \Delta v_{\text{FWHM}} / 1.665 \text{ km s}^{-1}$), 3.5 km s^{-1} , and 3.5 km s^{-1} for LkH α 101, AFGL 490, and Mon R2 IRS 3, respectively. The justification of the choice of the Doppler parameters will be discussed later in §4.2. The correction of the transmission efficiency was typically within $\pm 15 \%$ for the first overtone band, and from -10 to $+100 \%$ for the fundamental band.

The column density N_J in the lower state of a transition is related to the equivalent width W_λ with the following equation,

$$\frac{W_\lambda}{\lambda} = \frac{\pi e^2}{m_e c^2} N_J \lambda f$$

in the optically thin limit; where J is the rotational quantum number of the lower state, f is the oscillator strength of the transition. The other quantities have their usual meaning. However, since the instrumental resolution is much lower than the intrinsic line widths, it is not trivial to distinguish whether an absorption line is saturated or not. We deduced

the column density with a curve of growth analysis (Figure 3). Again we assumed the same Doppler parameters used in the calculation of transmission efficiency. The oscillator strengths were taken from Goorvitch & Chackerian (1994). For those objects, AFGL 490 and Mon R2 IRS 3, the equivalent widths of ^{13}CO were taken from Mitchell et al. (1995) and Giannakopoulou et al. (1997), and recalculated into the column densities with the curve of growth analysis. The equivalent width and the column density are summarized in Table 1 and Table 2.

3.2. Boltzmann Plot and Carbon Isotope Ratio

The abundance ratio of ^{12}CO to ^{13}CO is derived with no assumption on their excitation conditions, because numbers of absorption lines were detected from various rotational levels of ^{12}CO and ^{13}CO , which are in their vibrational ground states under the temperatures currently considered. The column density N_J in the rotational level J is proportional to the Boltzmann factor if the population distribution is expressed by a single excitation temperature T_{ex} ,

$$N_J = \frac{N}{Z(T_{\text{ex}})}(2J + 1) \exp\left(-\frac{E_J}{kT_{\text{ex}}}\right),$$

where N is the total column density of ^{12}CO or ^{13}CO , $Z(T) \approx kT/B_0$ is the partition function, and B_0 is the rotational constant that yields $E_J \approx B_0J(J + 1)$ with $B_0/k = 2.765$ and 2.644 K for ^{12}CO and ^{13}CO , respectively. When a line of sight is filled with the gas of a uniform excitation temperature, the Boltzmann plot, $\ln[N_J/(2J + 1)]$, has a linear dependence on E_J/k , with a slope representing the reciprocal of the excitation temperature, T_{ex}^{-1} . The Boltzmann plots for ^{12}CO $\nu = 2 \leftarrow 0$ and ^{13}CO $\nu = 1 \leftarrow 0$ are shown in Figure 4–6 for LkH α 101, AFGL 490, and Mon R2 IRS 3 with $b = 2.0$ km s $^{-1}$, 3.5 km s $^{-1}$, 3.5 km s $^{-1}$, as well as other representative Doppler parameters, respectively.

The plots for LkH α 101 with $b = 2.0$ km s $^{-1}$ are fit by the straight lines with $T_{\text{ex}}=52$ K and 30 K for ^{12}CO and ^{13}CO , respectively. The vertical separation roughly represents the isotope ratio. The plots are almost parallel to each other, indicating the isotopomers have similar temperatures, most likely sharing common physical location. For AFGL 490 and Mon R2 IRS 3, on the other hand, the data points are not represented by single straight lines but have breaks at $E_J/k \sim 50$ K. This indicates that each line of sight contains a mixture of gas with two different excitation temperatures, as reported by Mitchell et al. (1995) and Giannakopoulou et al. (1997). On closer inspection of the plots for LkH α 101 as well as the cooler parts of the plots for AFGL 490 and Mon R2 IRS 3, i.e, the section with $E_J/k < 50$ K, we notice that the data points are not parallel to each other, but the slopes

for ^{13}CO are almost twice as steep as those for ^{12}CO . The effect will be briefly discussed in §4.3.

The linear fit to the Boltzmann plot gives the excitation temperature and the column density in rotational states J . Then the total column density of each isotopomer is calculated from the equation above. The $^{12}\text{CO}/^{13}\text{CO}$ ratios for the cool and warm components are 137 ± 9 , 86 ± 49 , and 158 for LkH α 101, AFGL 490, Mon R2 IRS 3, respectively. The total column densities and the isotopic ratios are summarized in Table 3. The quoted uncertainties are formal 1σ errors. The uncertainty is not given for Mon R2 IRS 3, because no error evaluations are available in Giannakopoulou et al. (1997) for the equivalent widths of ^{13}CO absorption lines. The systematic errors to be discussed in §4.2 may exceed the formal ones, but hard to be estimated and are not included here.

3.3. Kinematics

There are two temperature components found in the line of sights toward AFGL 490 and Mon R2 IRS 3. The presence of warm gas ($T_{\text{ex}} > 100$ K) have been recognized in Orion BN and other young stellar objects with the high resolution spectroscopy of CO in absorption and in emission (Scoville et al. 1983; Mitchell et al. 1988, 1989, 1990; Brittain et al. 2003). We infer that the low- J absorption lines with lower excitation temperature mainly arise in the cold gas in a molecular core, while the warm gas is located closer to the central stars, heated by the collisions with the warm dust grains. In order to show the kinematic properties of the foreground gas, we plotted in Figure 7 the line centroid velocity and velocity width as a function of E_J/k for Mon R2 IRS 3. The absorption lines from the cold gas ($E_J/k < 100$ K) have the velocity of $v_{\text{LSR}} = 6\text{--}8$ km s $^{-1}$, which is a few km s $^{-1}$ blueshifted with respect to the cloud velocity of $v_{\text{LSR}} \approx 10.5$ km s $^{-1}$ (Tafalla et al. 1997; Giannakopoulou et al. 1997). The absorption lines from the warm gas ($E_J/k > 100$ K), on the other hand, have the velocity of $v_{\text{LSR}} = 3\text{--}5$ km s $^{-1}$. It is significantly blueshifted with respect to the cloud velocity. The velocity width tends to be larger for the warm gas ($\Delta v_{\text{FWHM}} > 20$ km s $^{-1}$) than for the cold gas ($\Delta v_{\text{FWHM}} = 17\pm 1$ km s $^{-1}$). These differences in the kinematical properties again support the presence of multiple gas components along the line of sight toward Mon R2 IRS 3: the warm gas is part of an outflow approaching us, presumably extending to the central star, while the cold gas is consistent with the quiescent gas located farther out. A similar trend was also found for AFGL 490.

4. Discussion

4.1. Local Carbon Isotope Ratio from CO

The molecular clouds we observed are located at 0.8–1.2 kpc away from the solar system toward the outer region of the Galactic plane (Racine & van den Bergh 1970; Herbig 1971; Brand & Blitz 1993). The distance to LkH α 101 is recently revised by Stine & O’Neal (1998) who suggested that the object belongs to the Taurus-Auriga complex 140 pc away from us. The present observation should therefore represent the local carbon isotope ratio at 8.5–9.5 kpc from the Galactic center. The results from the present work are compared with other CO observations in Figure 8.

There is an upward trend in the millimeter emission spectroscopy of $^{12}\text{C}^{18}\text{O}/^{13}\text{C}^{18}\text{O}$ increasing steadily from 24 of Sgr B2 to 65 of W3(OH) toward the edge of the Galactic plane (Langer & Penzias 1990). The global trend sets the local value of $^{12}\text{C}^{18}\text{O}/^{13}\text{C}^{18}\text{O}$ to 57 ± 5 at 8.5 kpc from the Galactic center. However, an apparent scatter is recognized in the isotopic ratio in the solar neighborhood. Most of these values are substantially higher than that is expected from the Galactic trend. In particular the present observation ($^{12}\text{CO}/^{13}\text{CO} = 86\text{--}158$) results in serious conflict with the local value by a factor of three at most. It is even larger than the benchmark of the solar system 4.5–4.7 Gyr ago ($^{12}\text{C}/^{13}\text{C} = 89$) which is tightly constrained by the measurement of the terrestrial isotopic ratio. In the following sections we will discuss the observational and astrophysical biases that may deviate the measurement of $^{12}\text{CO}/^{13}\text{CO}$ from the intrinsic isotopic ratio in a molecular cloud.

4.2. Sources of Observational Error

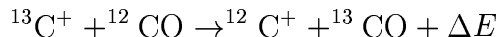
The poor cancellation of the atmospheric lines, over- and under-correction of the transmission efficiency, and the inaccuracy in the Doppler parameters, all introduce systematic errors in the column density measurement. The atmospheric effects are relatively minor as long as we have sufficient number of transitions to use simultaneously. The uncertain Doppler parameter, though, is the critical error source. The absorption line profile is not precisely a Gaussian in general as we had assumed, but may consist of sub-components, which are usually indistinguishable with modest spectral resolutions of near-infrared spectroscopy. The choice of the Doppler parameter b affects both on the calculation of the transmission efficiency and the curve of growth analysis. ^{13}CO fundamental transitions starting from the low- J rotational states are becoming optically thick. The error in b as much as $\pm 1 \text{ km s}^{-1}$ could change the analysis of the column density $N_J(^{13}\text{CO})$ by a factor of two at most for AFGL 490 (Figure 3).

The Doppler parameters can be estimated by (1) the deconvolution of the intrinsic line profile from the instrumental resolution of the near-infrared spectra, or (2) the high resolution ($\Delta v_{\text{FWHM}} < 1 \text{ km s}^{-1}$) radio spectroscopy toward the same targets. Mitchell et al. (1990, 1995) and Giannakopoulou et al. (1997) adapted $b = 3.5 \text{ km s}^{-1}$ for all three objects in the present study based on the above strategy. Their b values are consistent with more recent high-resolution radio spectroscopy within $\pm 1 \text{ km s}^{-1}$ (Choi et al. 2000; Schreyer et al. 2002). However, in the near-infrared method (1), the low resolution of the spectrograph ($\Delta v_{\text{FWHM}} \sim 10 \text{ km s}^{-1}$) usually hampers precise deconvolution of the b values. The radio emission spectroscopy (2), samples the gas with a large beam size. The line profiles are integrated within the entire field of view. It is most likely different from that of the single line of sight relevant to the near-infrared absorption spectroscopy. When a source is associated with an outflow, the radio emission spectroscopy counts both the foreground and background kinematic components in the same time, however, the near-infrared absorption spectroscopy is only sensitive to the foreground clouds. The absorption line profile could be significantly narrower than in the emission spectroscopy. The different optical depth in the different wavelengths also adds the uncertainty to the physical locations of the gas observed by radio and near-infrared spectroscopy, even they are in the same line of sight.

We tested the Doppler parameters in the following way. As described in §3.2, the logarithmic column density is a linear function of the E_J/k in the local thermodynamic equilibrium (LTE) condition. The large deviation of the data points from the straight line could be used as an indicator of that the Doppler parameter assumed in the curve of growth analysis is incorrect. In particular, R - and P -branch transitions starting from the same J level should give consistent column densities with each other. If the N_J derived from R - and P -branch disagrees over the measurement errors, it is most likely that the Doppler parameters in the curve of growth analysis was wrong. We present a series of the Boltzmann plots in Figure 4 for LkH α 101 constructed with different b values from 1.0 to 3.5 km s^{-1} . The slightly saturated ^{13}CO fundamental absorption lines could be a useful measure how good the estimation of b value is. For instance, the column density of ^{13}CO in $J = 0$ rotational state calculated with $b = 1.0 \text{ km s}^{-1}$ is apparently too high above the straight line that represents the LTE condition. On the other hand, the mismatch between the column densities calculated from the R - and P -branch transitions becomes larger in $J = 0$ –2 states when b is larger than 2.5 km s^{-1} . We infer the proper b value should be close to 2.0 km s^{-1} . The same plots for AFGL 490 and Mon R2 IRS 3 are shown in Figure 5 and Figure 6 for the range of $b = 1.5$ –4.0 km s^{-1} . We infer $b = 3.5 \text{ km s}^{-1}$ is the reasonable choice of the Doppler parameter for the both objects.

4.3. Astrophysical Biases

Chemical fractionation (Watson, Anicich, & Huntress 1976; Langer 1976, 1977; Langer et al. 1984; Liszt 1978) and the selective photodissociation (Bally & Langer 1982; Chu & Watson 1983; van Dishoeck & Black 1988; Warin, Benayoun, & Viala 1996) are the two major sources that bias $^{12}\text{CO}/^{13}\text{CO}$ from intrinsic carbon isotope ratio. For instance, the carbon isotope ratio measured in $\text{H}_2^{12}\text{CO}/\text{H}_2^{13}\text{CO}$ is usually higher (Henkel, Walmsley, & Wilson 1980; Henkel, Wilson, & Beiging 1982, 1983; Henkel, Güsten, & Gardner 1985) than that of $^{12}\text{CO}/^{13}\text{CO}$, which is attributed to the chemical fractionation of ^{13}C to CO (Langer et al. 1984). The following ion-molecule reaction



fractionates ^{13}CO as much as $\exp(\Delta E/kT)$ with $\Delta E/k$ being 35 K. The process is mostly effective in region where C^+ has significant population such as translucent clouds, surface of dense clouds, and close vicinity of embedded FUV sources. However, chemical fractionation decreases $^{12}\text{CO}/^{13}\text{CO}$, so cannot account for the present results.

For observations that give high $^{12}\text{CO}/^{13}\text{CO}$ ratios, the influence of selective photodissociation is possible. The carbon monoxide in a molecular cloud is protected by dust grains that attenuate the destructive FUV radiation from the interstellar and cloud internal sources. The ^{12}CO molecules, however, may become optically thick faster than the dust grains, though only at the photodissociative line absorption, to shield themselves efficiently. In contrast, the isotopomer ^{13}CO is less protected because of the smaller abundance. It is readily destroyed by the line and band absorption until it is protected by dust grains that place a continuum screen to the dissociative irradiation. The selective photodissociation therefore leads the higher $^{12}\text{CO}/^{13}\text{CO}$ ratio. In cases spatial variation of $^{12}\text{CO}/^{13}\text{CO}$ is apparent that decreases with the distance from the FUV sources (cloud surface or embedded hot stars), the selective photodissociation is a likely reason to account for the high $^{12}\text{CO}/^{13}\text{CO}$ ratio (S68 in Bally & Langer 1982; W3(OH) in Penzias 1983; Orion A in Langer 1993). The near-infrared technique inevitably requires embedded luminous sources in the line of sight. The influence of the photodissociation could be more important than in the radio emission observations. The higher isotope ratio $^{12}\text{CO}/^{13}\text{CO}$ in the warm component than the cool component in Mon R2 IRS 3 can be accounted by the selective photodissociation of ^{13}CO close to the central star.

However, the selective photodissociation is most effective in a cloud at about $A_V \leq 1$ mag, slightly before the dust grain extinction becomes completely thick (Chu & Watson 1983). It may be effective up to $A_V = 5\text{--}6$ mag in the strong UV radiation field in a giant molecular cloud (Langer & Penzias 1990). However, the elaborate calculations of $^{12}\text{CO}/^{13}\text{CO}$

by van Dishoeck & Black (1988) toward NGC 2024 IRS 2, a molecular cloud with high mass star forming region, does not show significant deviation from intrinsic carbon isotope ratio. The visible extinction toward LkH α 101, AFGL 490, and Mon R2 IRS 3 are $A_V = 10\text{--}12$ mag (Kelly, Rieke, & Campbell 1994; Aspin & Barsony 1994), $A_V = 25\text{--}40$ mag (Henning et al. 1984; Alonso-Costa & Kwan 1989) and $A_V = 30\text{--}70$ mag (Henning, Chini, & Pfau 1992; Preibisch et al. 2002), respectively. The ^{13}CO should be well protected by dust grains to make the selective photodissociation less effective. NGC 2264 is one of the most extensively studied sources for the carbon isotope ratio, but the measurements are still inconsistent with each other, or with the local average value (94 ± 18 by Penzias (1983), and 56 ± 3 by Langer & Penzias (1990) both with millimeter emission of C^{18}O ; 94 ± 13 by Mitchell & Maillard (1993) with near-infrared vibrational transition). Penzias (1983) concluded there is no evidence of selective photodissociation, because no spatial variation was found in the $^{12}\text{C}^{18}\text{O}/^{13}\text{C}^{18}\text{O}$ ratio. Mitchell & Maillard (1993) were also less inclined to favor selective photodissociation in NGC 2264 because the excitation temperature of the cloud is 25 K, indicating a well protected environment.

We note the temperature mismatch in ^{12}CO and ^{13}CO in cool section of the Boltzmann plots (Figure 4–6). We believe that this is because of photon trapping in the ^{12}CO rotational transition lines. Because the rotational transition of ^{12}CO is completely optically thick, the photon emission cannot escape from the cloud, but is re-absorbed by nearby molecules. The radiative cooling is no longer effective, the excitation temperature therefore goes up until it equilibrated with the collisional de-excitation with the surrounding hydrogen molecules. The population distribution in J states of the vibrational ground state should be in accord with the kinetic temperature of the ambient hydrogen molecules. In contrast, ^{13}CO is less abundant and optically thin. The photon trapping is less effective. The excitation temperature of ^{13}CO is therefore substantially cooler than the kinetic temperature of the hydrogen molecules with the lower bound set by the cosmic background radiation. Since the J -integrated total column density is proportional to the excitation temperature, the observed $^{12}\text{CO}/^{13}\text{CO}$ ratio is directly influenced by the twice higher excitation temperature of ^{12}CO ,

$$\frac{^{12}\text{CO}}{^{13}\text{CO}} = \frac{N_{J=0}(^{12}\text{CO}) T_{\text{ex}}(^{12}\text{CO})}{N_{J=0}(^{13}\text{CO}) T_{\text{ex}}(^{13}\text{CO})}.$$

On the other hand, most of the millimeter wavelength observations have been carried out in one or a few transitions of low- J states without direct measurements of the populations escaped in the high- J states or the rotational excitation temperature. The identical temperature is sometimes assumed in both isotopomers of ^{12}C and ^{13}C , or the temperatures are calculated relying on the radiation transfer models. The kinetic temperature of hydrogen is the weakest link of the model assumptions. The antenna temperature of ^{12}CO is often used as surrogate, which is not always the correct representation. Langer & Penzias (1990, 1993)

employed optically-thin $C^{18}O$ to circumvent large corrections for the different excitation conditions, nevertheless they noted that a reduction in the excitation temperature by 1 K could change the isotopic ratio by 6–9%. The further multi-transition observations carried out by the near-infrared spectroscopy could be the key to eliminate uncertainties in the excitation conditions, and to assess the isotope ratios without ambiguity.

5. Summary

We have presented the initial results from the near infrared CO isotope project toward the local molecular clouds. The high resolution near-infrared spectroscopy of $^{12}CO \nu = 2 \leftarrow 0$ and $^{13}CO \nu = 1 \leftarrow 0$ provides complimentary measurements of carbon isotope ratio to the radio and optical observations. We found $^{12}CO/^{13}CO = 137 \pm 9$, 86 ± 49 , and 158 for LkH α 101, AFGL 490, and Mon R2, respectively. The results are significantly higher than that is predicted by the local Galactic gradient previously reported in millimeter CO observations. Detailed comparison with isotope ratios measured with other tracers, in particular with CH^+ molecular ions, should be in order. The twice higher excitation temperature in ^{12}CO than ^{13}CO , presumably resulted from the photon trapping in ^{12}CO rotational transitions, may contribute to increase in $^{12}CO/^{13}CO$ ratio. The uncertainty in the Doppler parameters for the unresolved absorption lines is a crucial parameter needed to minimize the systematic errors. The selective photodestruction of ^{13}CO is not likely, however, the observed molecular clouds are well shielded with $A_V = 10\text{--}70$ mag, the photodissociation would not reconcile the isotopic conflict as much as factor of three.

We acknowledge all of the staff and crew of the Subaru Telescope and NAOJ for their valuable assistance in obtaining this data and their continuous support for the construction of IRCS and the adaptive optics system. We thank Sean Brittain and Craig Kulesa for their critical reading of the manuscript. We are grateful Jun'ichi Morino and Wako Aoki for helpful discussions with them. We wish to thank an anonymous referee for useful comments. M. G. is supported by a Japan Society for the Promotion of Science fellowship.

REFERENCES

- Alonso-Costa, J. L., & Kwan, J. 1989, *ApJ*, 338
- Anders, E., & Grevesse, N. 1989, *Geochim. Cosmochim. Acta*, 53, 197
- Aspin, C., & Barsony, M. 1994, *A&A*, 288, 849

- Audouze, J., Lequeux, J., & Vigroux, L. 1975, *A&A*, 43, 71
- Bally, J., & Langer, W. D. 1982, *ApJ*, 255, 143
- Bensch, F., Pak, I., Wouterloot, J. G. A., Klapper, G., & Winnewisser, G. 2001, *ApJ*, 562, L185
- Brittain, S. D., Rettig, T. W., Simon, T., Kulesa, C., DiSanti, M. A., & Dello Russo, N. 2003, *ApJ*, 588, 535
- Black, J. H., & Willner, S. P. 1984, *ApJ*, 279, 673
- Boreiko, R. T., & Betz, A. L. 1996, *ApJ*, 467, L113
- Brand, J., & Blitz, L. 1993, *A&A*, 275, 67
- Centurión, M., Càssola, C., & Vladilo, G. 1996, *A&A*, 302, 243
- Choi, M., Evans, N. J., II, Tafalla, M., & Bachiller, R. 2000, *ApJ*, 538, 738
- Chu, Y. -H., & Watson, W. D. 1983, *ApJ*, 267, 151
- Frerking, M. A., Wilson, R. W., Linke, R. A., & Wannier, P. G. 1980, *ApJ*, 240, 65
- Gaessler, W., et al. 2002, *Proc. SPIE*, 4494, 30
- Giannakopoulou, J., Mitchell, G. F., Hasegawa, T. I., Matthews, H. E., & Maillard, J. -P. 1997, *ApJ*, 487, 346
- Goorvitch, D., & Chackerian, C., Jr. 1994, *ApJS*, 91, 483
- Grevesse, N., Noels, A., & Sauval, A. J. 1996, in *ASP Conf. Ser. 99, Cosmic Abundances*, ed. S. S. Holt & G. Sonneborn (San Francisco: ASP), 117
- Hall, D. N. B., Ridgway, S. T., Gillet, F. C., & Kleinmann, S. G. 1978, *ApJ*, 223, L47
- Hawkins, I., Craig, N., & Meyer, D. M. 1993, *ApJ*, 407, 185
- Hawkins, I., & Jura, M. 1987, *ApJ*, 317, 926
- Henning, Th., Chini, R., & Pfau, W. 1992, *A&A*, 263, 285
- Henning, Th., Friedemann, C., Gürtler, J., & Dorschner, J. 1984, *Astr. Nachr.*, 305, 607
- Henkel, C., Güsten, R., & Gardner, F. F. 1985, *A&A*, 143, 148

- Henkel, C., Walmsley, C. M., & Wilson, T. L. 1980, *A&A*, 82, 41
- Henkel, C., Wilson, T. L., & Bieging, J. 1982, *A&A*, 109, 344
- Henkel, C., Wilson, T. L., Walmsley, C. M., & Pauls, T. 1983, *A&A*, 127, 388
- Herbig, G. H. 1971, *ApJ*, 169, 537
- Langer, W. D. 1976, *ApJ*, 210, 328
- Langer, W. D., 1977, *ApJ*, 212, L39
- Langer, W. D., Graedel, T. E., Frerking, M. A., & Armentrout, P. B. 1984, *ApJ*, 277, 581
- Langer, W. D., & Penzias, A. A. 1990, *ApJ*, 357, 477
- Langer, W. D., & Penzias, A. A. 1993, *ApJ*, 408, 539
- Liszt, H. S. 1978, *ApJ*, 222, 484
- Lord, S. D. 1992, NASA Technical Memoir 103957
- Keene, J., Schilke, P., Kooi, J., Lis, D. C., Mehringer, D. M., & Phillips, T. G. 1998, *ApJ*, 494, L107
- Kelly, D. M., Rieke, G. H., & Campbell, B. 1994, *ApJ*, 425, 231
- Kobayashi, N., et al. 2000, *Proc. SPIE*, 4008, 1056
- Mitchell, G. F., Allen, M., Beer, R., Dekany, R., Huntress, W., & Maillard, J. -P. 1988, *ApJ*, 327, L17
- Mitchell, G. F., Curry, C., Maillard, J. -P., & Allen, M. 1989, *ApJ*, 341, 1020
- Mitchell, G. F., Lee, S. W., Maillard, J. -P., Matthews, H., Hasegawa, T. I., & Harris, A. I. 1995, *ApJ*, 438, 794
- Mitchell, G. F., & Maillard, J. -P. 1993, *ApJ*, 404, L79
- Mitchell, G. F., Maillard, J. -P., Allen, M., Beer, R., & Belcourt, K. 1990, *ApJ*, 363, 554
- Penzias, A. A. 1980, *Science*, 208, 16
- Penzias, A. A. 1983, *ApJ*, 273, 195
- Prantzos, N., Aubert, O., & Audouze, J. 1996, *A&A*, 309, 760

- Preibisch, T., Balega, Y. Y., Schertl, D. & Weigelt, G. 2002, *A&A*, 392, 945
- Racine, R., & van den Bergh, S. 1970, in *IAU Symp. 38, The Spiral Structure of our Galaxy*, ed. W. Becker & G. Contopoulos (Dordrecht: Reidel), 219
- Rothman, L. S., et al. 1998, *J. Quant. Spectrosc. Radiat. Transfer*, 60, 665
- Savage, C., Apponi, A. J., Ziurys, L. M., & Wyckoff, S. 2002, *ApJ*, 578, 211
- Schreyer, K., Henning, Th., van der Tak, F. F. S., Boonman, A. M. S., & van Dishoeck, E. F. 2002, *A&A*, 394, 561
- Scoville, N., Klienmann, S. G., Hall, D. N. B., & Ridgway, S. T. 1983, *ApJ*, 275, 201
- Stahl, O., & Wilson, T. L. 1992, *A&A*, 254, 327
- Stahl, O., Wilson, T. L., Henkel, C., & Appenzeller, I. 1989, *A&A*, 221, 321
- Stein, P. C., & O'Neal, D. 1998, *AJ*, 116, 890
- Tafalla, M., Bachiller, R., Wright, M. C. H., & Welch, W. J. 1997, *ApJ*, 474, 329
- Takami, H., Takato, N., Otsubo, M., Kanzawa, T., Kamata, Y., Nakashima, K., & Iye, M. 1998, *Proc. SPIE*, 3353, 500
- Tieftrunk, A. R., Jacobs, K., Martin, C. L., Siebertz, O., Stark, A. A., Stutzki, J., Walker, C. K., & Wright, G. A. 2001, *A&A*, 375, L23
- Tokunaga, A. T., et al. 1998, *Proc. SPIE*, 3354, 512
- van Dishoeck, E. F., & Black, J. H. 1988, *ApJ*, 334, 771
- Vladilo, G., Centurión, M., & Càssola, C. 1993, *A&A*, 273, 239
- Wannier, P. G. 1980, *ARA&A*, 18, 399
- Watson, W. D., Anicich, V. G., & Huntress, W. T. 1976, *ApJ*, 205, L165
- Warin, S., Benayoun, J. J., & Viala, Y. P. 1996, *A&A*, 308, 535
- Wilson, T. L. 1999, *Rep. Prog. Phys.*, 62, 143
- Wilson, T. L., & Rood, R. T. 1994, *ARA&A*, 32, 191

Fig. 1.— The first overtone band of the vibrational transition of ^{12}CO at 2.296–2.353 μm for LkH α 101, AFGL 490 and Mon R2 IRS 3. The R - and P -branch absorption lines are marked with dotted vertical lines. The atmospheric transmission curve was computed with ATRAN code (Lord 1992) to highlight poor transmission regions. This allows us to distinguish the residual features.

Fig. 2.— The fundamental band of the vibrational transition of ^{13}CO at 4.714–4.824 μm for LkH α 101. The R - and P - branch absorption lines of ^{13}CO along with the high- J transitions of ^{12}CO are marked with dotted and dot-dashed verticals, respectively. The $R(1)$ transition of ^{13}CO is not included in the following analysis, because the line is completely blended with the $R(10)$ transition of ^{12}CO . The atmospheric transmission curve was computed with ATRAN code (Lord 1992) to highlight poor transmission regions.

Fig. 3.— The curve of growth analysis of AFGL 490. The column density calculation critically depends on the Doppler parameter b . The fundamental band is more saturated than the first overtone band, thus more sensitive to the b parameter we use. The error of $\Delta b = \pm 1.0 \text{ km s}^{-1}$ may influence the column density of the low- J rotational states by a factor of two at most.

Fig. 4.— The Boltzmann plots for LkH α 101 with different b values from 1.0 to 3.5 km s^{-1} . Under the LTE condition, the data points fall in a straight line, with the slope representing the reciprocal excitation temperature (T_{ex}^{-1}). The column densities obtained with the curve of growth analysis with $b = 2.0 \text{ km s}^{-1}$ most closely follows the straight lines of the LTE condition. We infer the proper value of b should be about 2.0 km s^{-1} , and the result obtained with $b = 2.0 \text{ km s}^{-1}$ will be referred in the following discussion. The error bars in the plots are $\pm 3 \sigma$. The vertical offset between two sequences represents the relative abundance of ^{12}CO to ^{13}CO . The isotopic ratio in the total column densities is $^{12}\text{CO}/^{13}\text{CO} = 137 \pm 9$. The quoted error is for 1 σ , but for the statistical noise only.

Fig. 5.— Same as Figure 4, but for AFGL 490 with a range of b from 1.5 to 4.0 km s^{-1} . Two temperature components are found which is divided at $E_J/k \sim 50 \text{ K}$. The data for the equivalent widths of $^{13}\text{CO } \nu = 1 \leftarrow 0$ is from Mitchell et al. (1995) re-converted to the column densities with the curve of growth analysis. The result obtained with $b = 3.5 \text{ km s}^{-1}$ is referred in the following discussion. The error bars in the plots are $\pm 3 \sigma$. The isotopic ratio is $^{12}\text{CO}/^{13}\text{CO} = 86 \pm 49$. The quoted error is for 1 σ , but for the statistical noise only.

Fig. 6.— Same as Figure 4, but for Mon R2 IRS 3 with a range of b from 1.5 to 4.0 km s^{-1} . At

least two temperature components are found which is divided at $E_J/k \sim 50$ K. The data for the equivalent widths of $^{13}\text{CO } \nu = 1 \leftarrow 0$ is from Giannakopoulou et al. (1997) re-converted to the column densities with the curve of growth analysis. The result obtained with $b = 3.5 \text{ km s}^{-1}$ is referred in the following discussion. The error bars in the plots are $\pm 3 \sigma$. The isotopic ratio is $^{12}\text{CO}/^{13}\text{CO} = 158$.

Fig. 7.— The offset of the line center and the line width of the ^{12}CO first overtone in Mon R2 IRS 3. The central wavelength of the absorption lines are blueshifted in the higher J transitions with the line width being larger. The line widths are given in FWHM without correcting the instrumental resolution. Together with the temperature, the line kinematics implies the warm component seen in the Boltzmann plot is an outflow initiated close to the central star.

Fig. 8.— The carbon monoxide isotope ratio as a function of the Galactocentric distance. Unmistakable trend is seen in the millimeter-wavelength emission observation of C^{18}O (Langer & Penzias 1990). The measurements toward Orion BN (Scoville et al. 1983) and NGC 2264 (Mitchell & Maillard 1993) utilize the near-infrared technique same as the present observation. The galactocentric distance in Langer & Penzias (1990) is scaled so that the solar system is relocated at 8.5 kpc from the Galactic center. The galactocentric distances to Mon R2 IRS 3 and AFGL 490 are both supposed to be 9.3 kpc. LkH α 101 is assumed to be located at 8.6 kpc. There is a substantial scatter in the measurements in the local molecular clouds within about 1 kpc of the sun.

Table 1. $^{12}\text{CO } \nu = 0 \rightarrow 2$ absorption lines.

$^{12}\text{CO } \nu = 0 \rightarrow 2$ Transition	E_J/k [K]	f [10^{-8}]	LkH α 101 ($b=2.0$ km/s)			AFGL 490 ($b=3.5$ km/s)			Mon R2 IRS 3 ($b=3.5$ km/s)		
			λ [μm]	W_λ^a [$10^{-6}\mu\text{m}$]	N_J [10^{17}cm^{-2}]	λ [μm]	W_λ^a [$10^{-6}\mu\text{m}$]	N_J [10^{17}cm^{-2}]	λ [μm]	W_λ^a [$10^{-6}\mu\text{m}$]	N_J [10^{17}cm^{-2}]
$P(2)\dots$	16.59	3.520	3.51801	6.02 \pm 0.34	3.79 \pm 0.24	2.351607	5.20 \pm 0.88	9.96 \pm 0.38	3.51866	2.67 \pm 0.70	5.89 \pm 0.61
$P(1)\dots$	5.53	9.9503	2.349465	13.28 \pm 0.61	10.23 \pm 0.52	3.49708	13.67 \pm 0.37	10.56 \pm 0.36	...
$R(0)\dots$	0.00	8.952	8.45448	4.63 \pm 0.20	1.13 \pm 0.03	3.45270	5.13 \pm 0.54	3.91 \pm 0.23	4.5512	17.40 \pm 0.46	4.59 \pm 0.14
5.53	6.0067	2.343222	20.74 \pm 2.11	8.43 \pm 1.07	2.343470	26.11 \pm 1.65	11.18 \pm 0.86	...
16.390	3.41414	7.17 \pm 0.37	3.00 \pm 0.28	3.41224	2.30 \pm 0.57	10.17 \pm 0.33	3.41477	31.60 \pm 0.45	5.86 \pm 0.30
339463	7.65 \pm 0.42	3.36 \pm 0.23	3.9256	24.29 \pm 0.49	11.82 \pm 0.33	3.9521	31.56 \pm 0.85	16.56 \pm 0.59
37341	20.11 \pm 0.47	9.63 \pm 0.28	3.7609	30.65 \pm 0.80	16.31 \pm 0.56
0 \pm 0.24	2.335735	30.59 \pm 0.74	16.50 \pm 0.54
06	27.66 \pm 0.75	14.58 \pm 0.54
24,68 \pm 0.56	2.70 \pm 0.35
02 \pm 0.58	11.07 \pm 0.35
0.47	10.27 \pm 0.30
7.83 \pm 0.18
27
29

^aAfter corrected for the transmission efficiency.

Table 2. $^{13}\text{CO } \nu = 0 \rightarrow 1$ absorption lines.

$^{13}\text{CO } \nu = 0 \rightarrow 1$ Transition	E_J/k [K]	f [10^{-6}]	LkH α 101 ($b=2.0$ km/s)		
			λ [μm]	W_λ^a [$10^{-5}\mu\text{m}$]	N_J [10^{15}cm^{-2}]
$P(6)\dots$	111.06	4.9700	4.823291	0.72 ± 0.13	0.74 ± 0.10
$P(4)\dots$	52.89	4.8044	4.805587	2.17 ± 0.13	2.57 ± 0.19
$P(3)\dots$	31.73	4.6414	4.796850	2.38 ± 0.08	2.97 ± 0.12
$P(2)\dots$	15.87	4.3420	4.788271	2.88 ± 0.14	4.02 ± 0.26
$P(1)\dots$	5.29	3.6233	4.779755	2.41 ± 0.06	3.90 ± 0.12
$R(0)\dots$	0.00	10.9200	4.763114	2.82 ± 0.24	1.58 ± 0.08
$R(2)\dots$	15.87	6.5740	4.746863	3.18 ± 0.05	3.07 ± 0.05
$R(3)\dots$	31.73	6.2743	4.738887	2.29 ± 0.14	2.16 ± 0.18
$R(4)\dots$	52.89	6.1111	4.731028	2.07 ± 0.07	1.97 ± 0.08
$R(5)\dots$	79.33	6.0118	4.723267	1.35 ± 0.13	1.24 ± 0.14

^aAfter corrected for the transmission efficiency.

Table 3. Summary of total column density.

	LkH α 101 ($b=2.0$ km/s)	AFGL 490 ($b=3.5$ km/s)			Mon R2 IRS 3 ($b=3.5$ km/s)		
		cool	warm	total	cool	warm	total
$T_{\text{ex}}(^{12}\text{CO})$ [K]	52 ± 3	36 ± 3	143 ± 11		49 ± 3	252 ± 8	
$T_{\text{ex}}(^{13}\text{CO})$ [K]	30 ± 1	16 ± 5	164 ± 101		26	277	
$N(^{12}\text{CO})$ [10^{16}cm^{-2}]	184 ± 11	333 ± 28	400 ± 67	732 ± 73	483 ± 32	1194 ± 73	1677 ± 80
$N(^{13}\text{CO})$ [10^{16}cm^{-2}]	1.34 ± 0.04	3.01 ± 1.25	5.52 ± 4.68	8.80 ± 4.80	7.21	10.63	
$^{12}\text{CO}/^{13}\text{CO}$	137 ± 9	111 ± 45	72 ± 62	86 ± 49	141	166	158

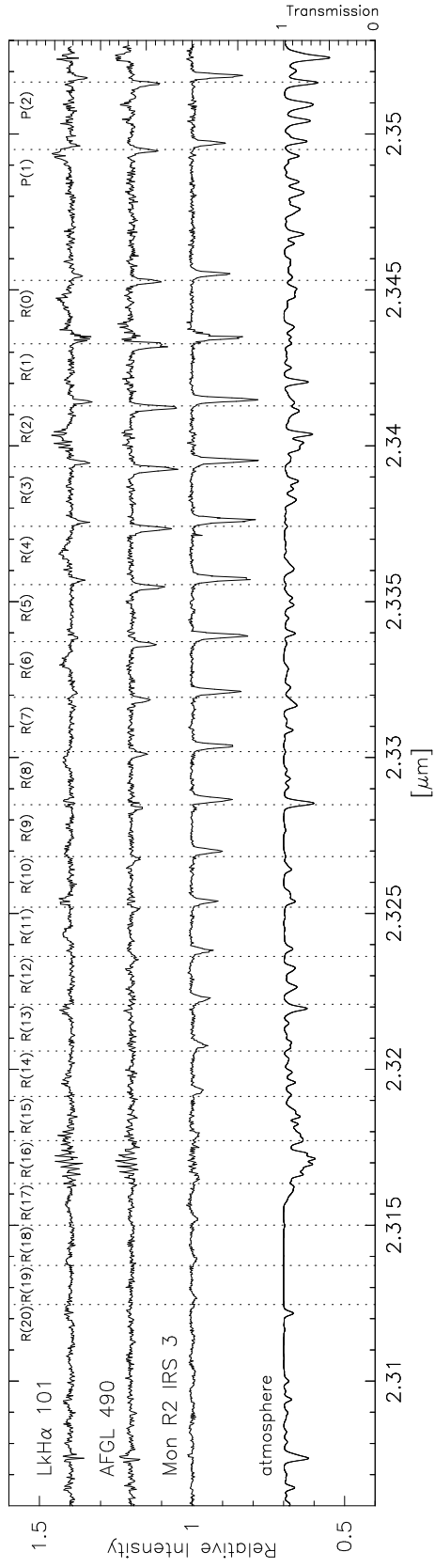


Fig. 1.—

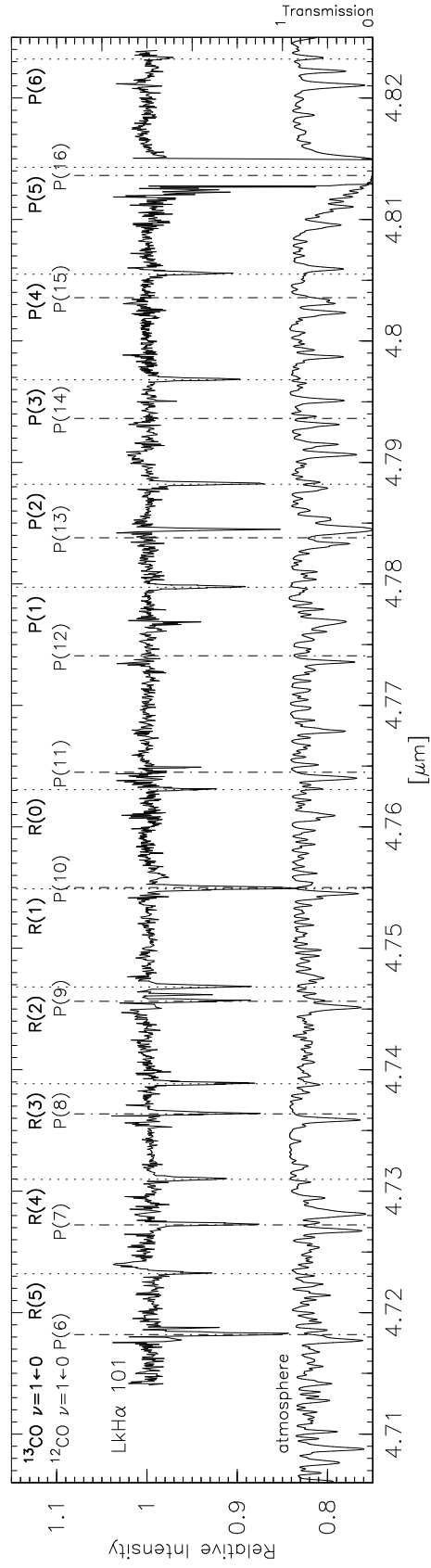


Fig. 2.—

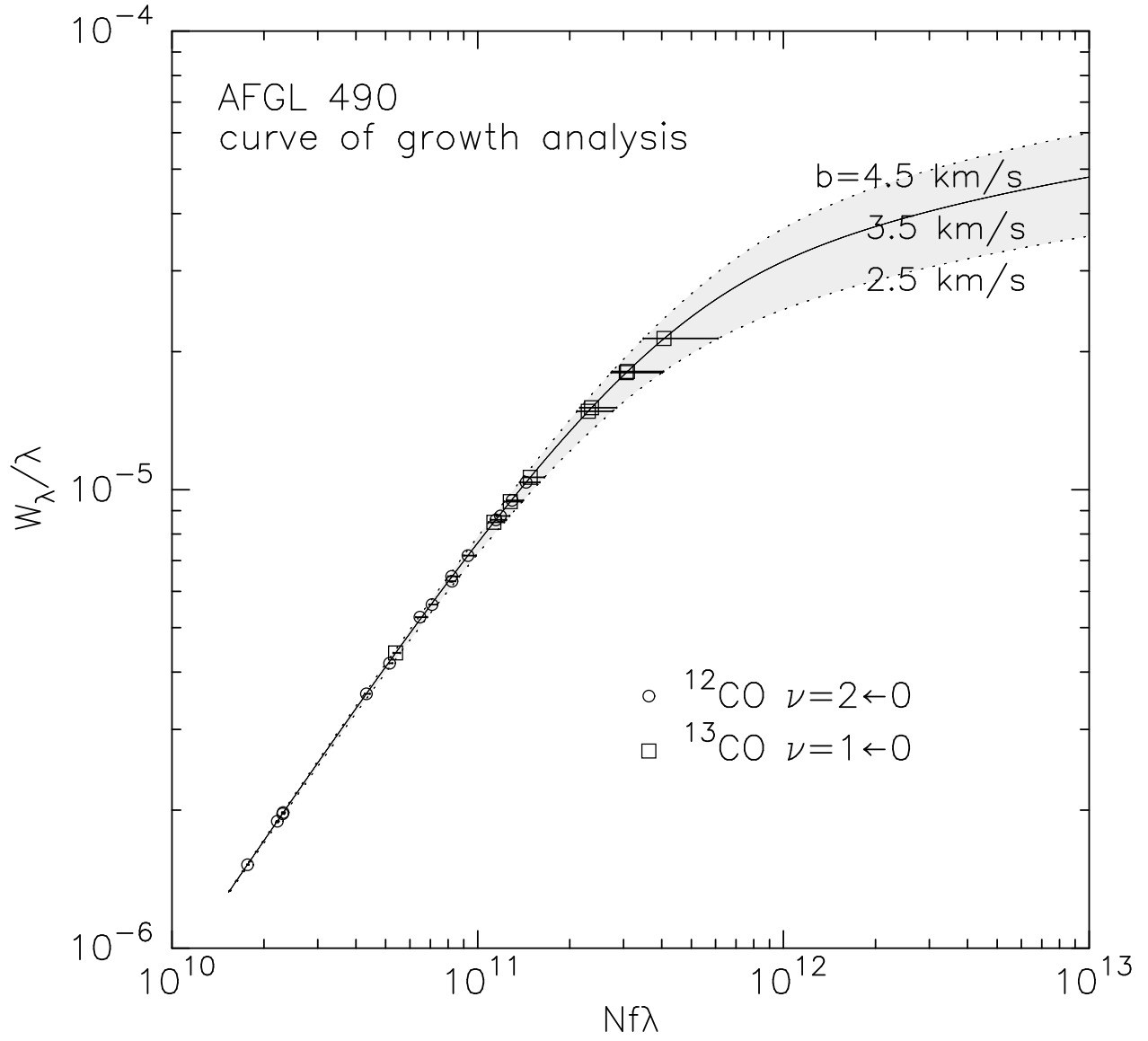


Fig. 3.—

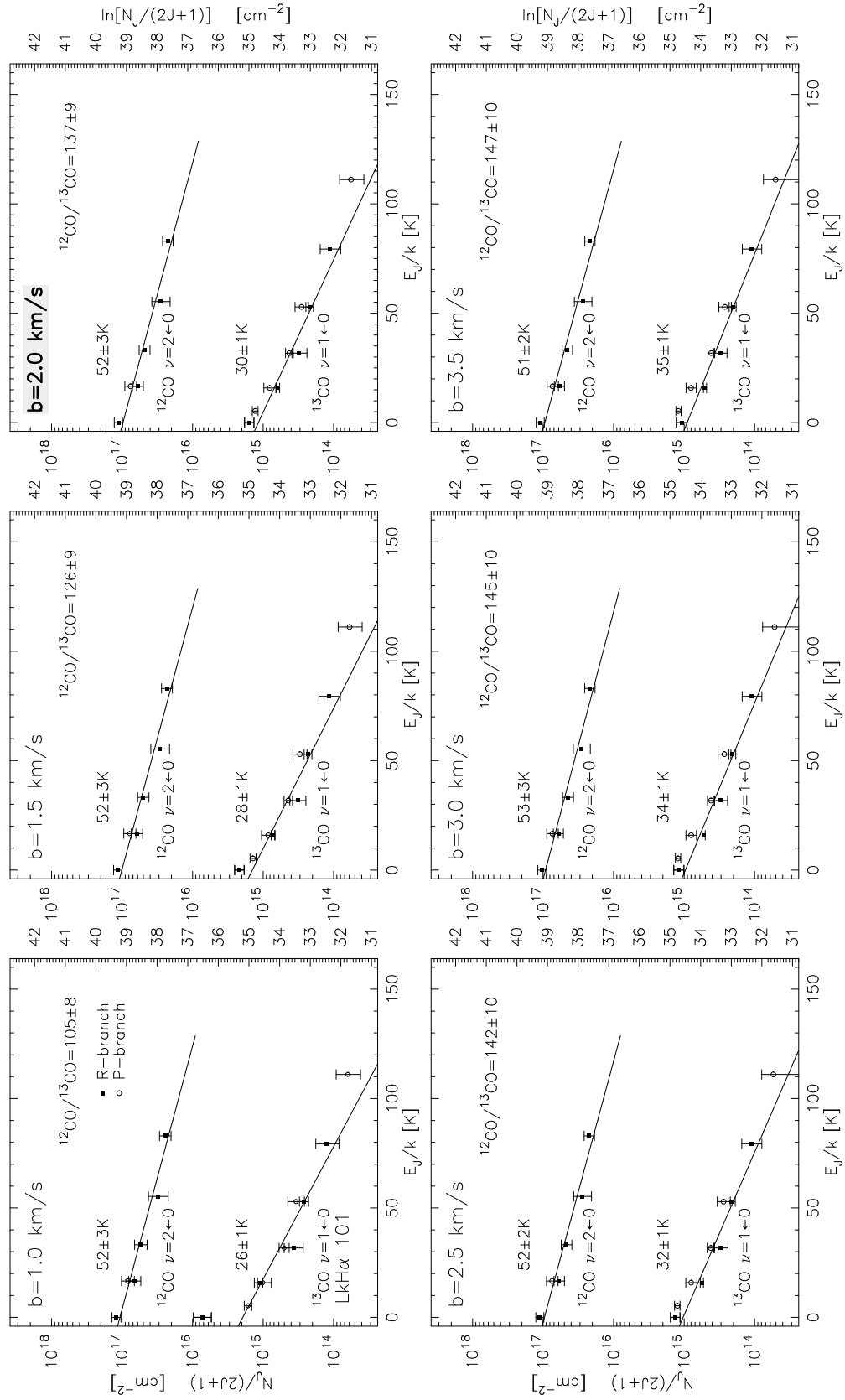


Fig. 4.—

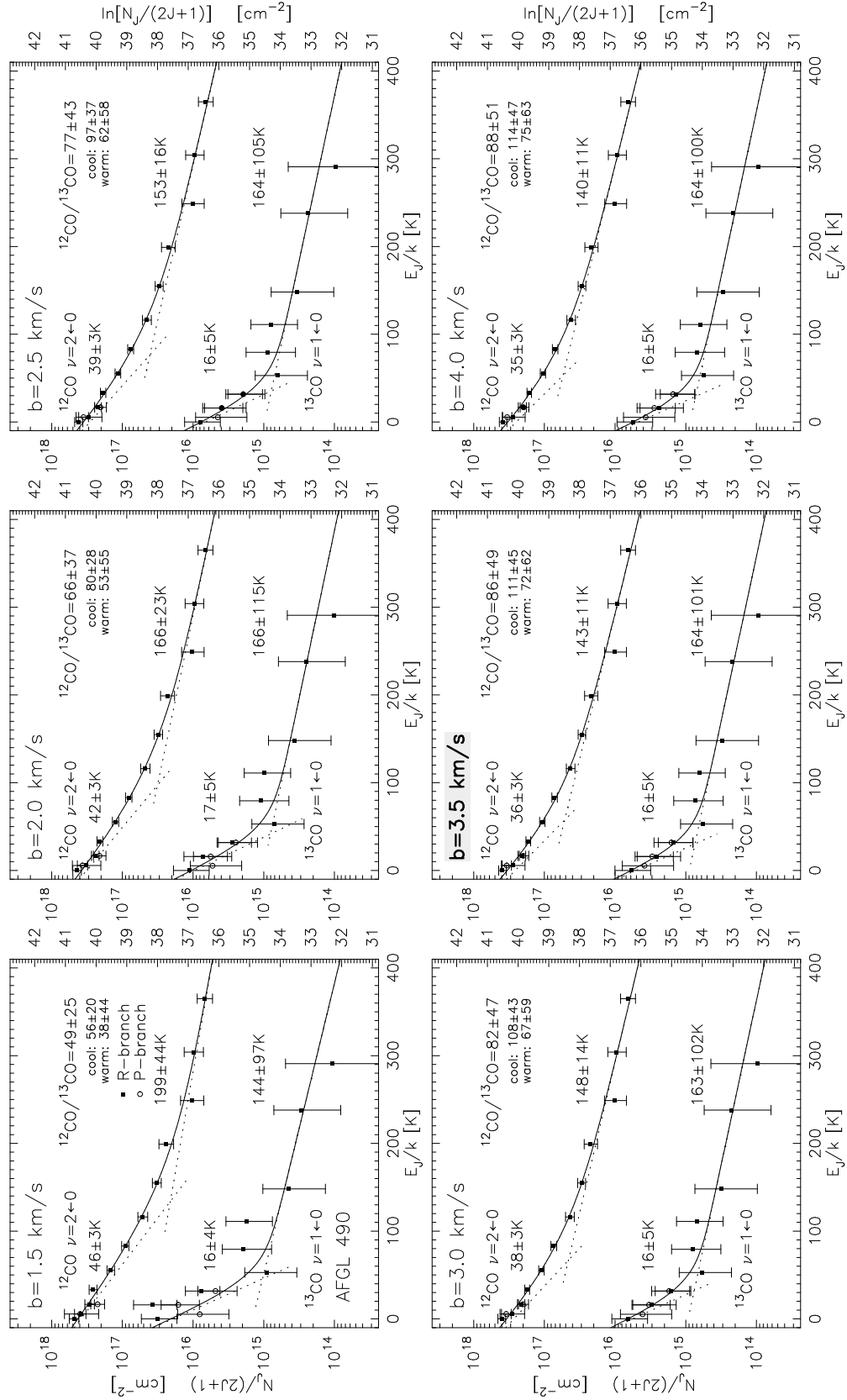


Fig. 5.—

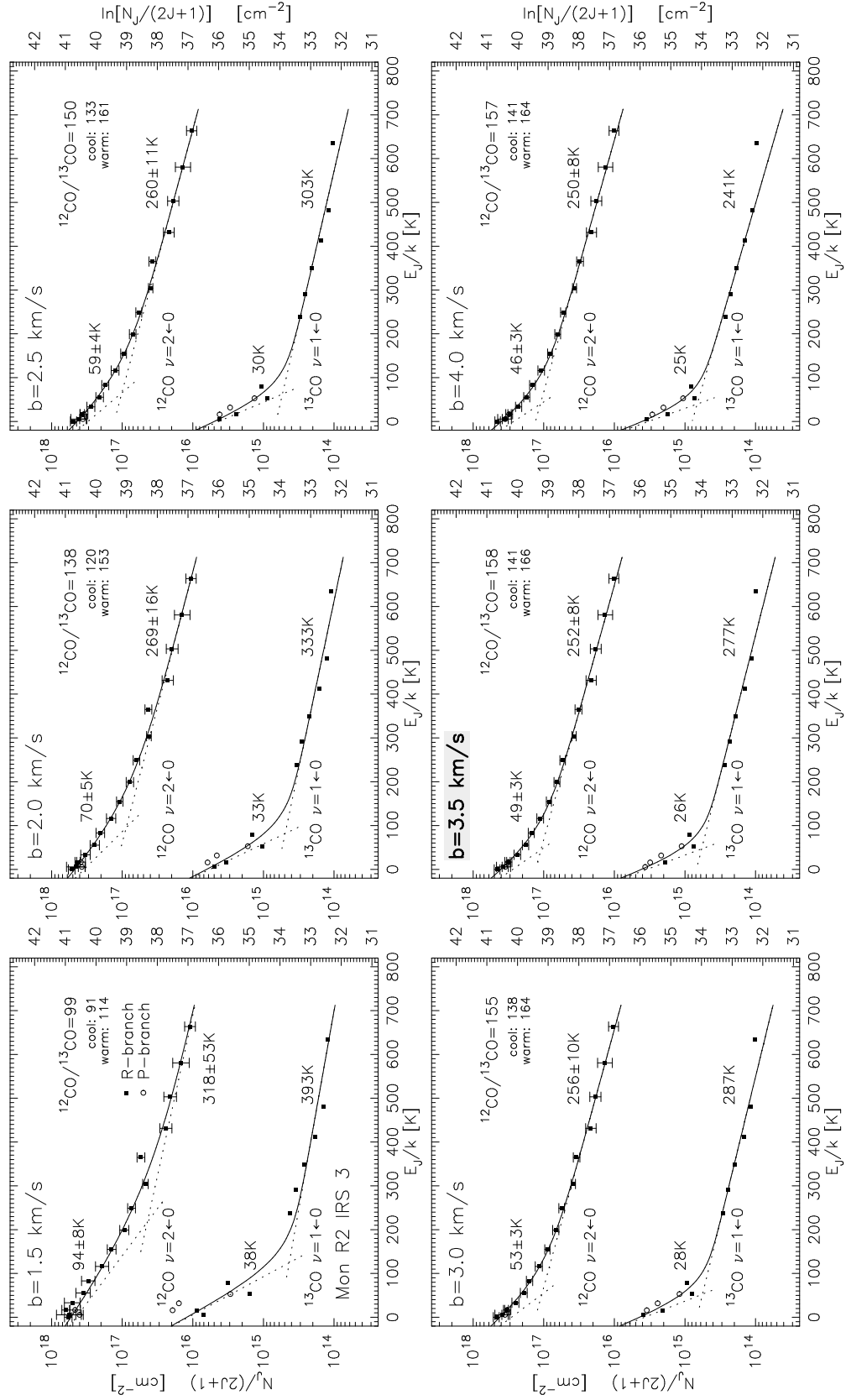


Fig. 6.—

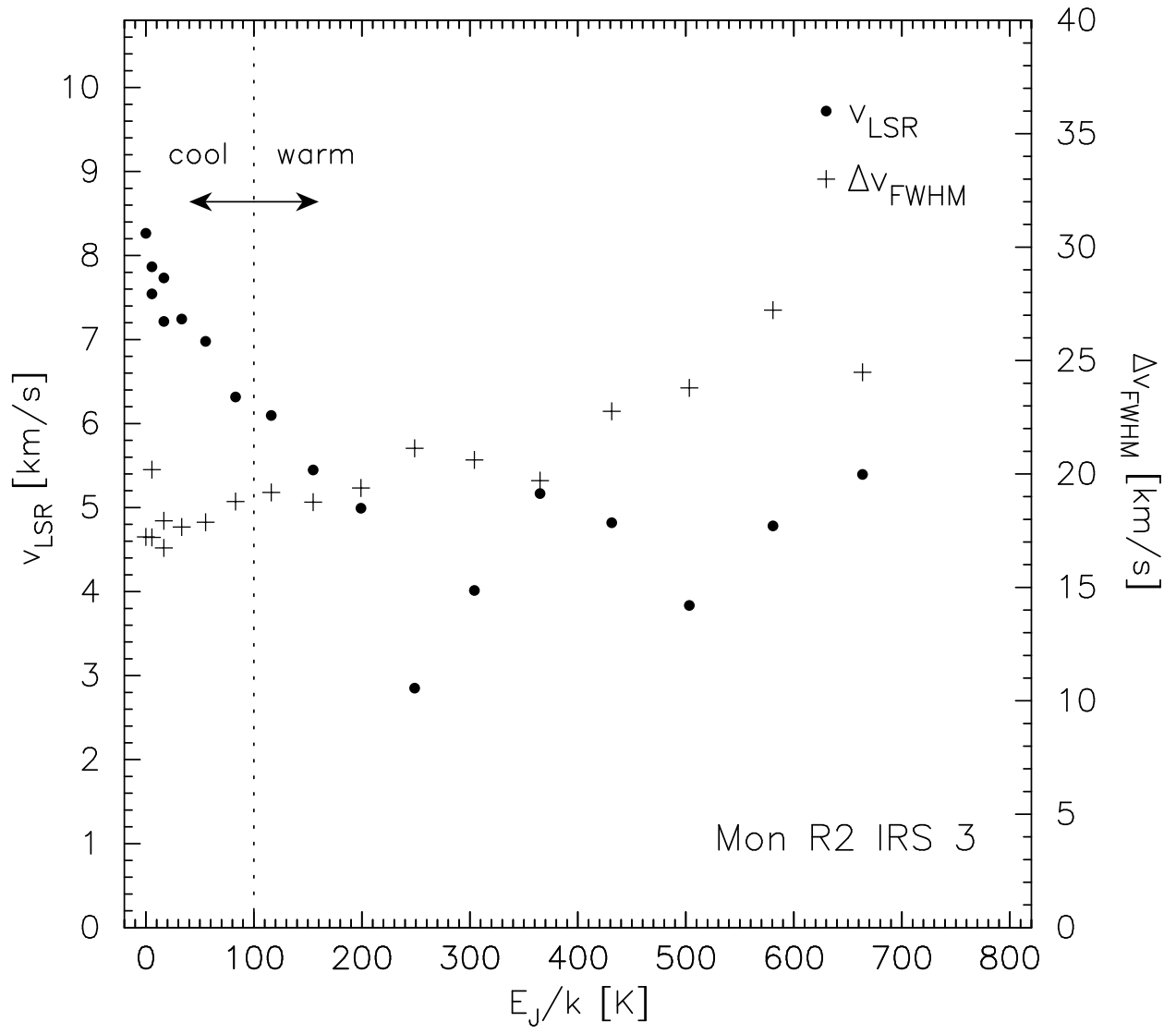


Fig. 7.—

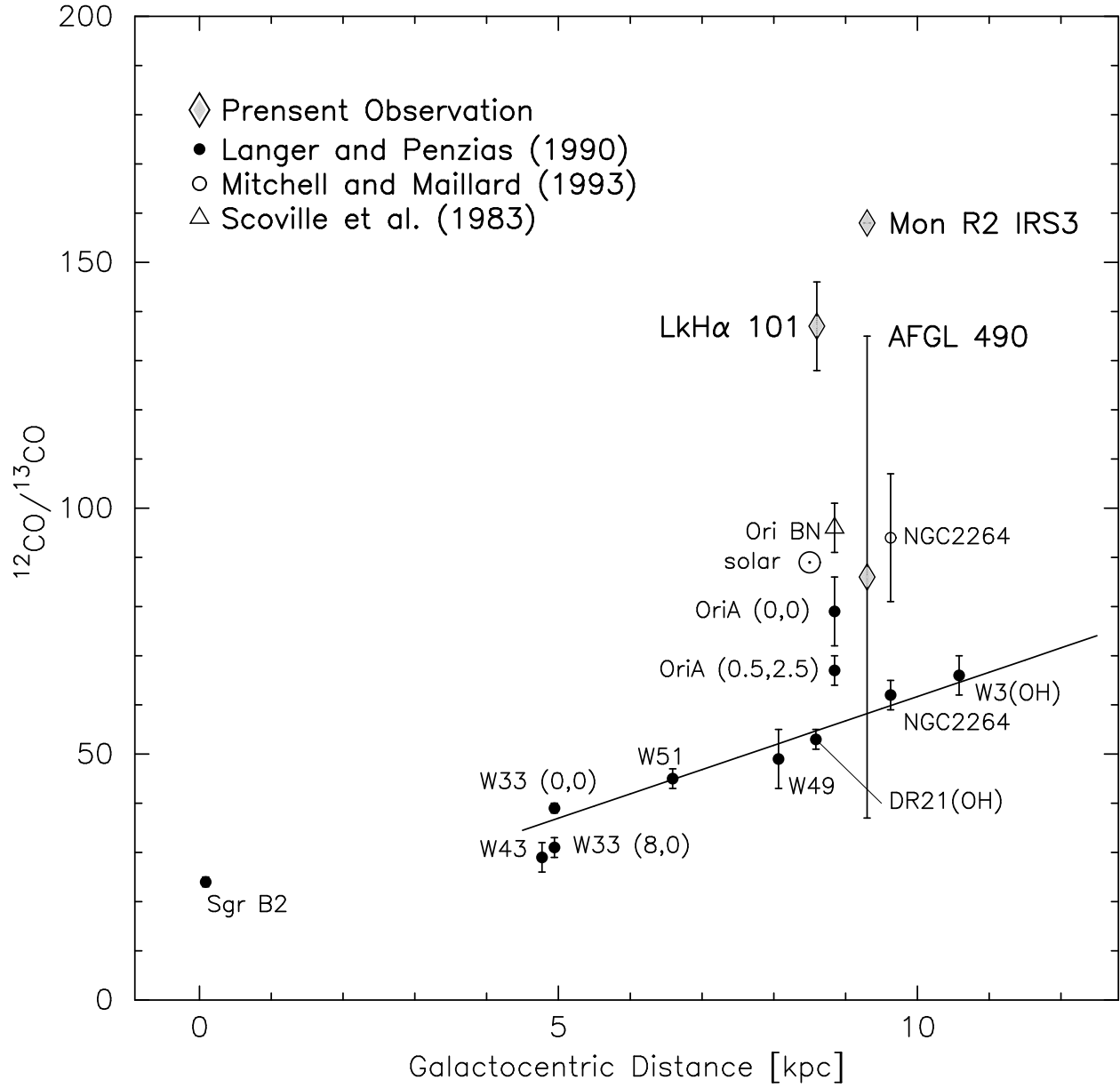


Fig. 8.—